Volume 1 | Number 1 | Jan 2013 | Pages 1–100

Journal of
Materials Chemistry A

Materials for energy and sustainability
www.rsc.org/materialsA

Li+

ROYAL SOCIETY
OF CHEMISTRY

ROYAL SOCIETY
OF CHEMISTRY

www.rsc.org/materialsA

Journal of Materials Chemistry A

Dynamic Article Links ▶

ARTICLE TYPE

Self-Assembled Wafer-like Porous NaTi$_2$(PO$_4$)$_3$ Decorated with Hierarchical Carbon as a High-Rate Anode for Aqueous Rechargeable Sodium Batteries

Baidan Zhao[a,‡], Qiuyue Wang[a,‡], Sen Zhang*[b], Chao Deng*[a]

Three-dimensional (3D) hierarchical porous structure is ideal for constructing high-performance electrode materials, which offers such advantages as large surface area, stable structural integrity and efficient ionic transport. In this report, we prepare a novel wafer-like 3D porous structured NaTi$_2$(PO$_4$)$_3$/C by a facile self-assembled strategy. The NaTi$_2$(PO$_4$)$_3$ crystal is not only coated by a nanoscale carbon
10 layer but also embedded in a microscale carbon network, which self-assembles into secondary particle in a plate-like shape. The hierarchical carbon in platelike particle constitutes 3D porous framework with bicontinuous electronic conductive skeleton, showing a wafer-like structure. When used as anode in aqueous system, the wafer-like composite exhibits better sodium intercalation kinetics and enhanced high-rate capability than nonporous samples. Moreover, a full aqueous rechargeable sodium battery is fabricated using wafer-like NaTi$_2$(PO$_4$)$_3$ as anode and Na$_{0.44}$MnO$_2$ as cathode. The cell exhibits superior high rate property and ultralong-life performance,
15 which delivers 64% of the capacity at 30 *C* and retains 67% of the capacity after 400 cycles at alternate 50 and 5 *C*. In view of the high efficient electron/ion transport pathways and robust structure stability, the wafer-like structure is put forwards as a new strategy of nanoarchitecture tailoring to achieve high-performance electrodes.

KEYWORDS: wafer-like porous architecture; hierarchical carbon decoration; rate capability; aqueous sodium rechargeable battery

20 1 Introduction

The fast development of renewable and sustainable energy resources such as solar, wind and tide needs safe and affordable stationary energy storage. Various kinds of battery chemistry from conventional lead acid, nickel metal hydride to advanced
25 lithium ion battery have been proposed as possible candidates[1-4]. However, the disadvantages such as insufficient durability, safety and limited resource restrict their applications. Aqueous rechargeable alkali-metal ion (Li$^+$, Na$^+$) batteries come into sight as a promising candidate since introduced by Dahn's group in
30 1994[5]. The high conductivity and good safety make it a good alternative for large-scale applications. Particularly, the aqueous rechargeable sodium battery (ARSB) attracts more attention than its lithium counterpart from a practical aspect due to the low cost and high natural abundant of sodium[6,7].

35 The electrochemical properties of ARSB are determined by electrode materials. Various materials such as oxides[8], polyanions[9], prussian blue analogues[10] and so on have been identified as electrode materials for ARSB. Most recently, Qian's group reported a new ARSB system based on NaMnO$_2$, which
40 exhibits high energy density and good cycling stability[11]. However, the species of anode materials are much narrower than those of the cathode materials. Up to now, only a few materials have been applicable as anode in ARSB[6,12-14]. Among them, NASICON-type NaTi$_2$(PO$_4$)$_3$ (NTP) is a representative one[11,15-19].
45 The super sodium ionic conductor structure and open framework provides 3D sodium intercalation pathways internal NaTi$_2$(PO$_4$)$_3$ crystal, which results in its high theoretical capacity of 133 mAh·g^{-1} and well-defined redox potential of -0.6 V (vs. SHE)[15-19]. However, facing the same problems as other polyanion materials,
50 NaTi$_2$(PO$_4$)$_3$ suffers from the poor electronic conductivity, which severely restricts its ion intercalation kinetic and high rate capability.

The improvement of electronic conductivity can be achieved in three ways, *i.e.* conductive carbon (or graphene, carbon
55 nanotube) coating[20,21], nanotailoring[22,23] and cations doping[24-26]. Among them, carbon coating is the most economic and feasible technique. However, traditional carbon coating only provides single electron pathways surrounding individual particles. It leads to the poor connectivity between randomly distributed particles,
60 which induces inconsecutive electron transport pathways and restricts the high-rate property[20,27]. Constructing graphene or carbon nanotube hybrid structure modifies the poor connection between individual particles[28-30]. However, it is at the expanse of volume energy density due to the insufficient compaction

between loose graphene nanosheets (or carbon nanotube). Therefore, it is necessary to design more effective strategies, which could offset the defects in traditional strategies and make breakthrough for high-performance electrode materials.

Three-dimensional (3D) porous structure shows great superior in energy applications[31-35]. The advantages such as high surface area, good contact with electrolyte and high structure stability result in its superior ion transport kinetic and good cycling stability. Moreover, as the shape of secondary particle is carefully controlled, the fatal defect of insufficient volume energy density for porous structure would be offset. In the family of 3D porous structure, a special branch, *i.e.* the carbon-based porous structure, has attracted particular attention[20,33-35]. It coupled the advantages of high conductive framework of carbon matrix and good electrolyte penetration of porous architecture, resulting in the high-efficient electron/ion transport. Therefore, it has been considered as an effective strategy to construct high-performance electrode.

Following this viewpoint, for the first time, we designed a new structure, named "hierarchical carbon decorated wafer-like porous architecture" for $NaTi_2(PO_4)_3$, and it can be also applied to other polyanion materials as well. A facile self-assembled method is employed to fabricate the wafer-like porous structure. The glycine is used as chelating agent, polyethylene glycol (PEG600) is used as soft temple, and citric acid is used as carbon source. As illustrated in Figure 1, the $NaTi_2(PO_4)_3$ crystal are decorated with hierarchical carbon, *i.e.* the nanoscale carbon coating and the microscale carbon network, which aggregates into a secondary particle in platelike shape. The hierarchical carbon not only provides bicontinuous conductive network for fast electron transport, but also constructs high porous structure for high efficient electrolyte percolation. Both advantages are favorable to fast charge transfer reaction. Meanwhile, the hierarchical carbon also acts as a buffering protective shell, which stabilizes the crystal upon cycling. Based on the internal 3D porous framework together with the outside plate-like particle morphology, the wafer-like structure is constructed for the $NaTi_2(PO_4)_3$/C composite.

Inspired by these advantages, the sodium intercalation chemistry of wafer-like porous $NaTi_2(PO_4)_3$/C composite is investigated in present study. The superior high rate property, enhanced sodium diffusion capability and good cycling stability of prepared material demonstrate the high efficiency of wafer-like structure in practical applications.

2 Experimental

2.1 Synthesis.

All the reagents were used without further purifying. The wafer-like $NaTi_2(PO_4)_3$/C composite (NTP/C-W) was prepared by a self-assembled synthesis. The starting materials are tetrabutyl titanate, glycine, citric acid, polyethylene glycol (PEG600), sodium bicarbonate, $NH_4H_2PO_4$, H_2O_2 and ammonia. Firstly, stoichiometric amount of tetrabutyl titanate was dissolved
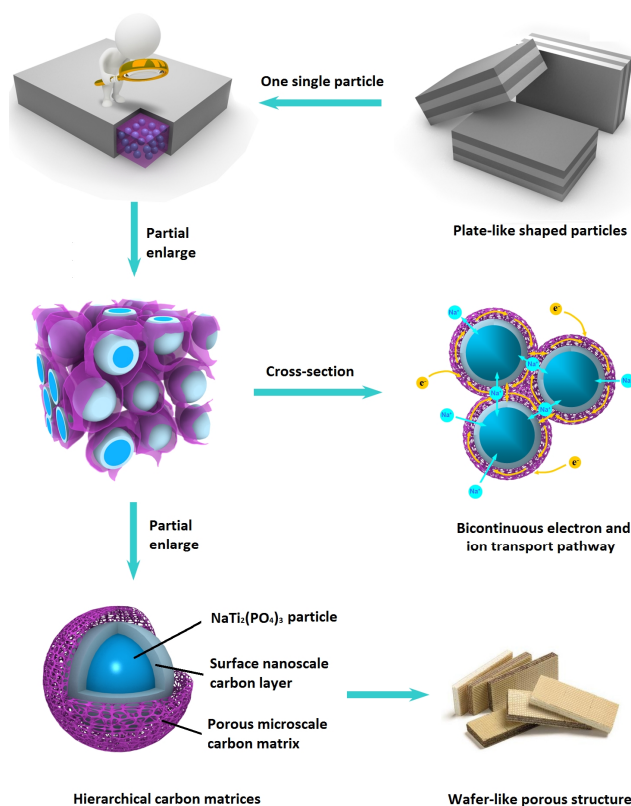

Figure 1 Scheme of wafer-like porous $NaTi_2(PO_4)_3$/C composite decorated by hierarchical carbon. The partial enlarged image illustrates the hierarchical carbon. The cross-section image illustrates the bicontinuous electron transport pathways.

into H_2O_2 (30%) solution under vigorously stirring. Then the ammonia was mixed into the solution, followed by the mixture of $NaHCO_3$ and $NH_4H_2PO_4$. After that, glycol, citric acid and PEG600 were added into the resultant solution. The mixed solution was kept stirring at 80 ^oC for 40 hours. Then the transport gel was transferred into an oven and dried at 140 ^oC overnight to produce the precursor. Finally, the resultant precursor was annealed at 700 ^oC for 8 hours at a heating rate of 2 $^oC \cdot min^{-1}$ in an argon atmosphere.

For comparison, the carbon-free pure $NaTi_2(PO_4)_3$ (NTP-P) was prepared in a manner similar to that of wafer-like porous sample, except for the absence of glycine and PEG600 during sol-gel process, and the calcination condition is transferred to 800 ^oC for 20 hours in air. The simple-carbon coated $NaTi_2(PO_4)_3$ (NTP/C-S) was prepared by re-sintering the mixture of pure $NaTi_2(PO_4)_3$ (NTP-P) and sucrose in argon atmosphere at 800 ^oC for 2 hours.

2.2 Materials characterization

Powder X-ray diffraction (XRD, Bruker D8/Germany) using Cu Kα radiation was employed to identify the crystalline phase of the material. The experiment was performed by using step mode
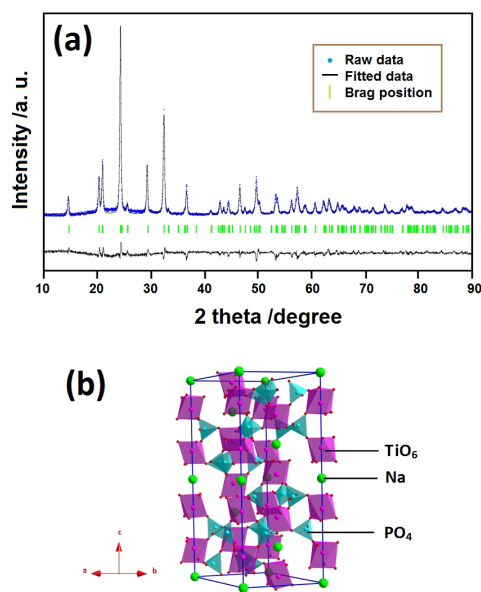
Figure 2 (a) XRD patterns of wafer-like porous NaTi$_2$(PO$_4$)$_3$/C composite. (b) Schematic illustration of crystal structure for NaTi$_2$(PO$_4$)$_3$. Units of TiO$_6$, PO$_4$ and sodium are displayed by different colors.

with a fixed time of 3 s and a step size of 0.02^o. The XRD pattern was refined by using the Rietveld method. The morphology was observed with a scanning electron microscope (SEM, HITACHIS-4700) and a transmission electron microscope (TEM, JEOS-2010 PHILIPS). Raman spectra were recorded with a Labram HR-800 (HORIBA JobinYvon) spectrometer by exciting a 514.5 nm Ar ion laser. Nitrogen adsorption-desorption isotherms were measured using a Micromeritics ASAP 2010 sorptometer and specific surface area and pore size distribution were calculated correspondingly. Carbon contents of the samples were determined by an element analyzer (EA, Elementar Vario EL).

2.3 Electrochemical measurements

Each composite electrode was made from a mixture of the active material, carbon black and polytetrafluoroethylene (PTFE) in a weight ratio of 80:10:10. The mixture was pressed into nickel foam and then dried at 80 ^{o}C for 12 hours in air. The effective area of each electrode is 1 cm^2. The de/intercalation mechanism of sodium ion was evaluated in 1M Na$_2$SO$_4$ electrolyte with Ag/AgCl electrode as reference. The aqueous rechargeable sodium battery was assembled using Na$_{0.44}$MnO$_2$ as cathode and NaTi$_2$(PO$_4$)$_3$ composite as anode. The Ag/AgCl electrode was employed as reference electrode to monitor the potential of each electrode upon galvanostatic cycling of the full cell. Cyclic voltammetry (CV) were measured in a Zivelab electrochemical workstation. Galvanostatic charge/discharge tests were conducted on a LAND battery testing system (Wuhan, China).

3 Results and Discussion

The crystal structure of prepared NaTi$_2$(PO$_4$)$_3$/C composite is indentified by XRD patterns. As displayed in Figure 2a, all diffraction peaks can be indexed to NASICON structure with $R\bar{3}c$ space group (167), indicating its high purity. The calculated lattice parameters of a=8.4938 (7) Å and c=21.8505 (0) Å are obtained based on Rietveld refinement. The detailed atomic parameters are listed in Table S1, which are coincided with the previous reported values[15-19]. Figure 2b illustrates the crystal structure of NaTi$_2$(PO$_4$)$_3$. Two TiO$_6$ octahedra and three PO$_4$ tetrahedra units interlinked via corners to construct the basic unit of [Ti$_2$(PO$_4$)$_3$] framework. Two types of interstitial sites (M1 and M2) coexist in the rhombohedral symmetry, and sodium ions fully occupy the M1 sites[15-17]. The open 3D framework of NASICON structure facilitates sodium ion transport, resulting in its good ionic mobility. Therefore, NaTi$_2$(PO$_4$)$_3$ is a good host for sodium intercalation, which is usually limited by the poor electronic conductivity.

The morphology and microstructure of prepared wafer-like NaTi$_2$(PO$_4$)$_3$/C composite are investigated by SEM and TEM observations. As displayed in Figure 3 (a~c), the composite exhibits two-dimensional platelike shaped particle with the width of 3~5 μm and the thickness of 0.5~1 μm. The cross-section image of one platelike particle evidences its internal porous architecture (Figure 3d). As shown in the enlarged image of cross-section (Figure 3e), the primary particles of the wafer-like composite are in the range of 30 to 50 nm, which are uniformly embedded in the porous carbon matrix (Figure 3f). The more detailed understanding of microstructure is provided by TEM observation. As displayed in Figure 3 (g and h), pieces of carbon sheets connect to each other and construct a large microsized carbon matrix. The nanosized NaTi$_2$(PO$_4$)$_3$ primary particles uniformly distributed inside the carbon matrix, resulting in a porous structure internal the platelike particle. The porous structure not only facilitates electrolyte penetration into the particles, but also is favorable to fast ion transport. Therefore, both the outside platelike morphology and the internal 3D porous structure construct the wafer-like architecture for the NaTi$_2$(PO$_4$)$_3$ composite. The detailed structure of nanosize primary particle is further indentified by high-resolution TEM (HRTEM). As shown in Figure 3(i), the well-resolved lattice fringe with the interplanar distance of 0.6100 nm corresponding to the (012) lattice planes of NaTi$_2$(PO$_4$)$_3$, indicating its single crystal nature. Moreover, a residual carbon layer of 3~5 nm is clearly observed on the surface of the particle, which constructs a high conductive layer surround the particle surface. Based on the nanoscale surface conductive layer and the microscale 3D conductive matrix, it constitutes bicontinuous pathways for fast electron transport. Given the high efficient electron and ion transports, the wafer-like architecture is favorable to fast electrochemical kinetic in "rocking-chair" chemistry.

Raman spectroscopy is recorded to further characterize the nature of carbon in the wafer-like NaTi$_2$(PO$_4$)$_3$/C composite. Two characteristic signatures located at ~1358 and 1590 cm^{-1} are
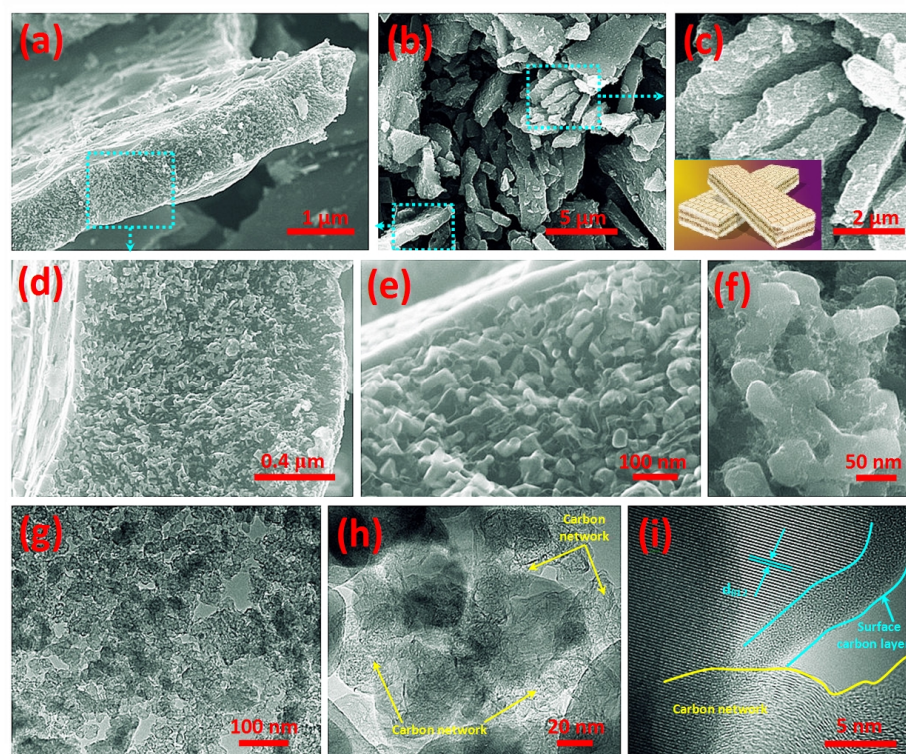
Figure 3 Morphology of the wafer-like porous $NaTi_2(PO_4)_3$/C composite: (a, b, c) SEM images of the wafer-like particles, (d, e, f) enlarged cross-section images of the wafer-like particle, (g, h) low-resolution TEM image of the wafer-like particle, (i) HRTEM image of one primary particle decorated by hierarchical carbon.

observed for the composite (Figure 4a), corresponding to the *D* (disordered carbon) and *G* (graphene carbon) bands[36]. The large *D* peak and high intensity ratio of *D/G* intensity ratio indicate the *in-situ* carbon in the composite is mainly amorphous state. The porous structure of wafer-like composite is investigated by nitrogen sorption isotherms. As displayed in Figure 4b, significant hysteresis loop in Brunauer-Emmet-Teller (BET) isotherm indicates the high porous structure of the composite. A high specific surface area of 69.7 m^2 g^{-1} and large pore volume of 0.282 cm^3 g^{-1} are obtained for the wafer-like porous composite.

In order to clarify the advantage of wafer-like architecture, two reference samples, *i.e.* carbon-free $NaTi_2(PO_4)_3$ (NTP-P) and the simple carbon-coated $NaTi_2(PO_4)_3$/C (NTP/C-S), are employed in this study. The physical characteristics of all the samples are summarized in Table S2. Both reference samples have single-phase structure without impurity (Figure S1). As compared in Figure 4(b,c), the BET surface of simple carbon-coated sample (NTP/C-S) is 26.1 m^2 g^{-1}, which is only about one third of the value for the wafer-like one. Extremely, the BET value of carbon-free sample (NTP-P) is as low as 5.8 m^2 g^{-1}. Meanwhile, the pore volumes of both reference samples are also much lower than the wafer-like one. The low BET areas and pore volumes of both reference samples are associated with their solid nature with low porosity (Figure S2). The above results demonstrate the superiority of high porous structure and large electrolyte/electrode interface area in the wafer-like sample.

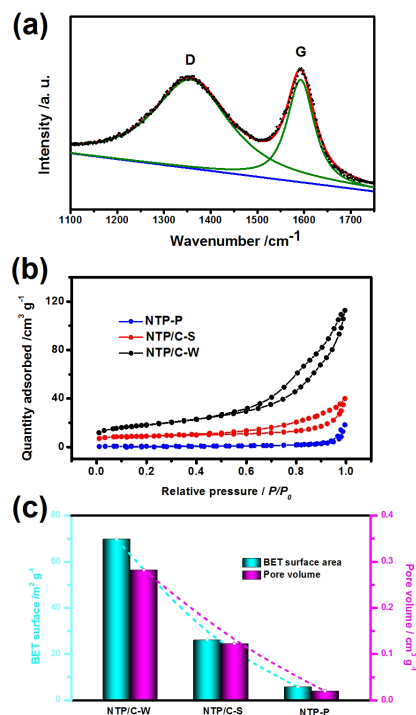Figure 4 (a) Raman spectroscopy of wafer-like porous $NaTi_2(PO_4)_3$/C composite. (b) Nitrogen sorption isotherms, (c) BET surfaces and pore volumes of the pure (NTP-P), simple carbon coated (NTP/C-S) and wafer-like (NTP/C-W) samples.
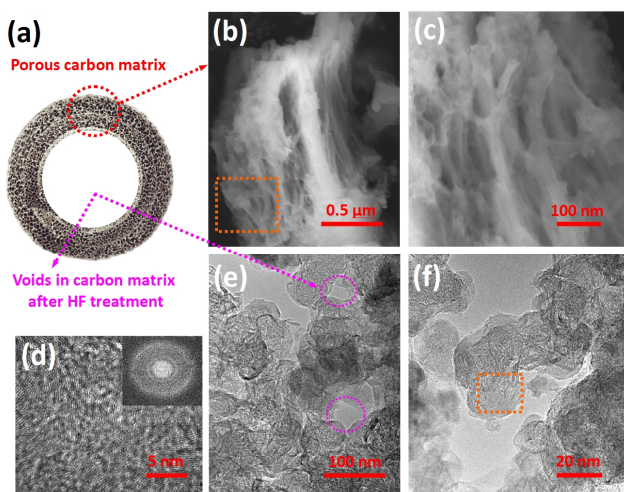
Figure 5 (a) Schematic image of pure carbon matrix in wafer-like $NaTi_2(PO_4)_3/C$ composite after HF treatment. (b,c) SEM and (d~f) TEM images of pure carbon matrix. The red square in (b) and (f) are respectively enlarged in (c) and (d). Voids in carbon matrix after HF treatment are emphasized by purple circle in (e). The corresponding FFT patterns are shown as inset of (d).

Based on above results, the hierarchical carbon plays an important role in the porous structure of wafer-like sample. Therefore, it is necessary to carefully investigate the structure of the carbon matrix. To obtain pure carbon matrix, the wafer-like composite is dipped into hydrofluoric acid along with intermittently ultrasonic treatment to complete remove $NaTi_2(PO_4)_3$ crystals. The morphology of wafer-like structure is largely remained after HF treatment (Figure 5b). The energy-

dispersive X-ray (EDS) analysis (Figure S3) demonstrates the $NaTi_2(PO_4)_3$ crystals have been totally removed and only carbon remains. The BET surface of residual carbon matrix is as high as 973 m^2 g^{-1} with a large pore volume of 1.53 cm^3 g^{-1}. SEM and TEM images (Figure 5 b~f) confirm that the 3D continuous and porous structure for the carbon matrix. Moreover, the voids of ~40 nm are observed in the carbon matrix, which is coincided with the size of crystal particles in the wafer-like architecture. Obviously, there are two major differences in the voids between the original wafer-like sample (Figure 3g) and the pure carbon matrix after HF treatment (Figure 5e). Firstly, the size of voids in the original wafer-like sample is in a wider range from several nanometers to nearly one hundred nanometers; while the size distribution of voids in pure carbon matrix is much narrower and most concentrates on ca. 40 nm. Secondly, the shape of voids in the original wafer-like sample is random, while that for the carbon matrix is much regular. Therefore, the regular and uniform voids can be attributed to the removal of $NaTi_2(PO_4)_3$ crystals after HF treatment. The above results demonstrate that the carbon matrix in the wafer-like composite has continuous framework and 3D porous architecture (Figure 5a). The $NaTi_2(PO_4)_3$ crystals are uniformly embedded in the carbon matrix and tightly contact with the carbon scaffolds. The porous carbon matrix not only provide continuous conductive framework for fast electron transport, but also enables easy electrolyte accessibility to promote ion transport. Both are favorable to fast ion intercalation kinetics during high rate charge/discharge.

The superior sodium intercalation kinetic of wafer-like composite over the references samples, *i.e.* the simple carbon coated sample and the pure sample, is demonstrated by CV results. Firstly, their sodium extraction/insertion processes are
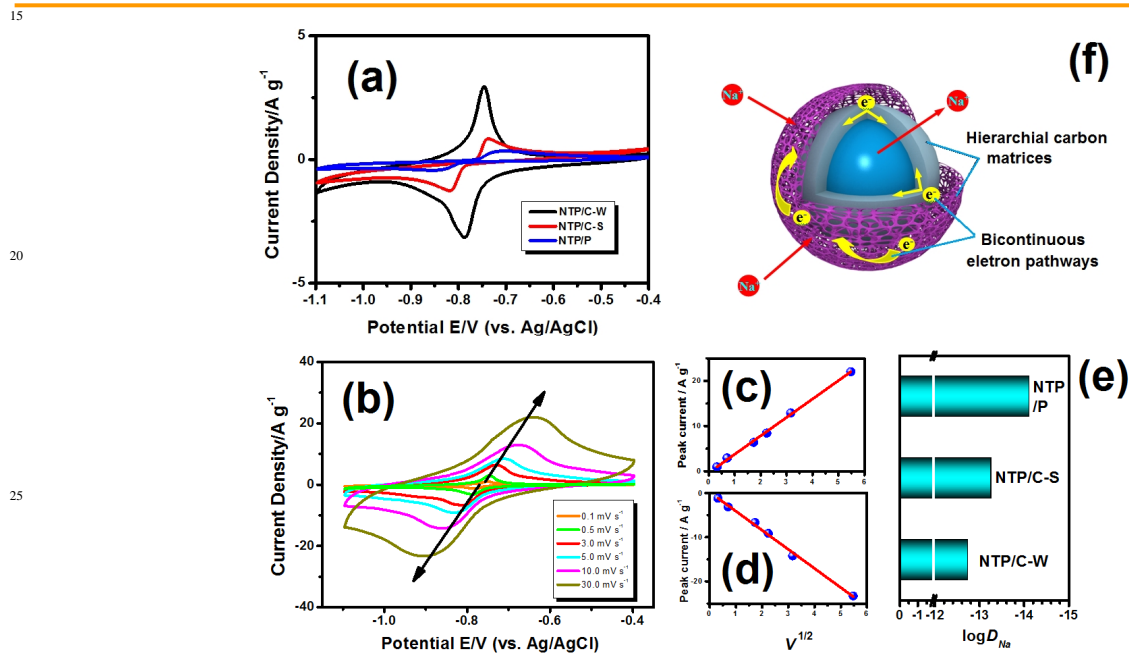

Figure 6 (a) CV curves of the pure (NTP-P), simple carbon coated (NTP/C-S) and wafer-like (NTP/C-W) samples at the scan rate of 0.5 mV s^{-1}. (b) CV curves of the wafer-like sample at various scan rates from 0.1 to 30 mV s^{-1} and (c,d) the peak current vs. square root of scan rate plots. (e) Comparison of sodium diffusion coefficients of all the samples. (f) Schematic image of bicontinuous pathways for high-efficient electron/ion transport in the wafer-like architecture is also illustrated.
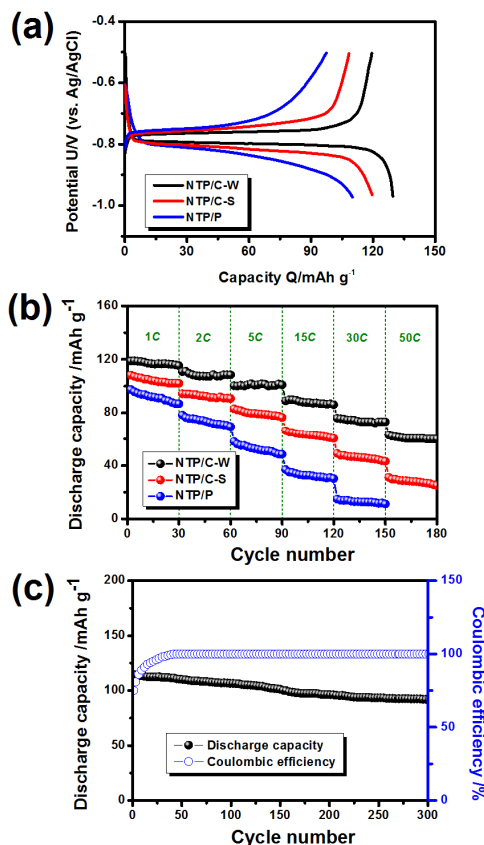
Figure 7 (a) Galvanostatic charge/discharge curves of the pure (NTP-P), simple carbon coated (NTP/C-S) and wafer-like (NTP/C-W) samples at 1 *C* rate. (b) Comparison of their rate capability at the current densities from 1 *C* to 50 *C*. (c) Long term cycling property of the wafer-like sample (NTP/C-W) at the 2 *C* rate for 300 cycles.

investigated by comparing the CV curves at the scan rate of 0.5 mV s^{-1}. As displayed in Figure 6(a), a pair of redox peaks is observed for each sample, corresponding to the insertion/extraction reaction in NaTi$_2$(PO$_4$)$_3$ crystal (equation 1).

$$NaTi_2(PO_4)_3 + 2Na^+ + 2e^- \xrightleftharpoons[charge]{discharge} Na_3Ti_2(PO_4)_3 \quad (1)$$
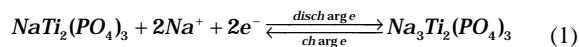
The strong and well-defined redox peaks of wafer-like composite indicate its good redox reversibility between Ti^{3+} and Ti^{4+}. As compared with the wafer-like material, much lower peak currents with larger redox potential difference are observed for the references materials, indicating their poor sodium intercalation kinetic. In order to clarify their ion intercalation capability, the sodium diffusion coefficients (D_{Na}) of all the samples were calculated. As displayed in Figure 6(b), CV curves are measured at various scan rates from 0.1 to 30 mV s^{-1}. The current peak intensities of all the materials decrease as increasing the scan rate. There is a linear relationship between the anodic/cathodic peak current and the square root of scan rate (Figure 6c,d), indicating that the controlling step of sodium intercalation process is sodium-ion diffusion. Therefore, the diffusion coefficient of sodium-ion can be calculated on the basis of the Randles-Sevcik equation (2)[37],

$$i_p = 0.4463(\frac{F^3}{RT})^{1/2} n^{3/2} A D_{Na}^{1/2} C^* v^{1/2} \quad (2)$$

Where i_p, n, A, C^* and v are the peak current, number of exchanged electrons, surface area, sodium concentration and sweep rate, respectively. As compared in Figure 6(e), the average diffusion coefficient (D_{Na}) for the wafer-like composite (NTP/C-W) is much higher than the simple carbon coated one (NTP/C-S) and the carbon-free pure one (NTP-P). The larger sodium diffusion coefficient demonstrates the faster sodium ion transport kinetics in the wafer-like structure. As illustrated in Figure 6(f), the wafer-like structure takes the advantage of both hierarchical porous structure and bicontinuous electron transport pathways, which facilitates fast electron/ion transport and is favorable to its ion intercalation kinetics. Therefore, it is demonstrated to be highly efficient to construct wafer-like structure for polyanion materials to achieve superior electrochemical kinetics.

The electrochemical properties of wafer-like NaTi$_2$(PO$_4$)$_3$/C composite and the reference samples are investigated. Firstly, the galvanostatic charge/discharge characteristics under different current rates (*i.e.* 1*C*, 2*C*, 5*C*, 15*C*, 30*C,* 50*C*) are studied. The wafer-like composite exhibits higher capacities than the reference samples at each current density. As displayed in Figure 7(a), a specific capacity of 119.4 mAh g^{-1} with flat potential plateau is obtained for the wafer-like sample (NTP/C-W) at the 1*C* rate. However, the capacities of only 108.3 and 97.5 mAh g^{-1} with sloping potential plateaus are obtained for the simple carbon coated (NTP/C-S) and pure samples (NTP-P) at the 1*C* rate. Moreover, the difference between the wafer-like composite and the reference materials is enlarged as the current density increases (Figure 7b). At the 50 *C* rate, the wafer-like sample delivers capacity of 63 mAh g^{-1}, corresponding to 50.3% of the capacity for 1 *C* rate. But the simple carbon coated sample only exhibits 31 mAh g^{-1}, corresponding to 28.6% of its 1 *C* capacity. Extremely, the carbon free sample delivers the capacity as low as 14.9 mAh g^{-1} at the 30 *C* rate and almost no capacity is obtained at the 50 *C*. The results demonstrate the superior rate capability of wafer-like composite, which can be attributed to its improved ion intercalation kinetic induced by both high conductivity and high porous structure in the wafer-like architecture. Moreover, wafer-like composite shows better cycling stability than the reference samples, which demonstrates the protective effect of hierarchical carbon as buffer layer for NaTi$_2$(PO$_4$)$_3$ crystals during cycling. The long-term cycling performance of the wafer-like sample is demonstrated in Figure 7(c). An initial capacity of 114 mAh g^{-1} with the coulombic efficiency of 75% is obtained in the first cycle. The insufficient columbic efficiency can be attributed to the hydrogen evolution at low voltage, and similar phenomenon is also observed in previous reports[11,15-19]. The increase of columbic efficiency accompanies the decrease of capacity as increases the cycle number. After three hundred cycles, a stable capacity of 92 mAh g^{-1} with nearly 100% coulombic efficiency is obtained. The result demonstrates the good cycling stability of prepared wafer-like NaTi$_2$(PO4)$_3$, which is associated with its special designed architecture and hierarchical carbon decoration.
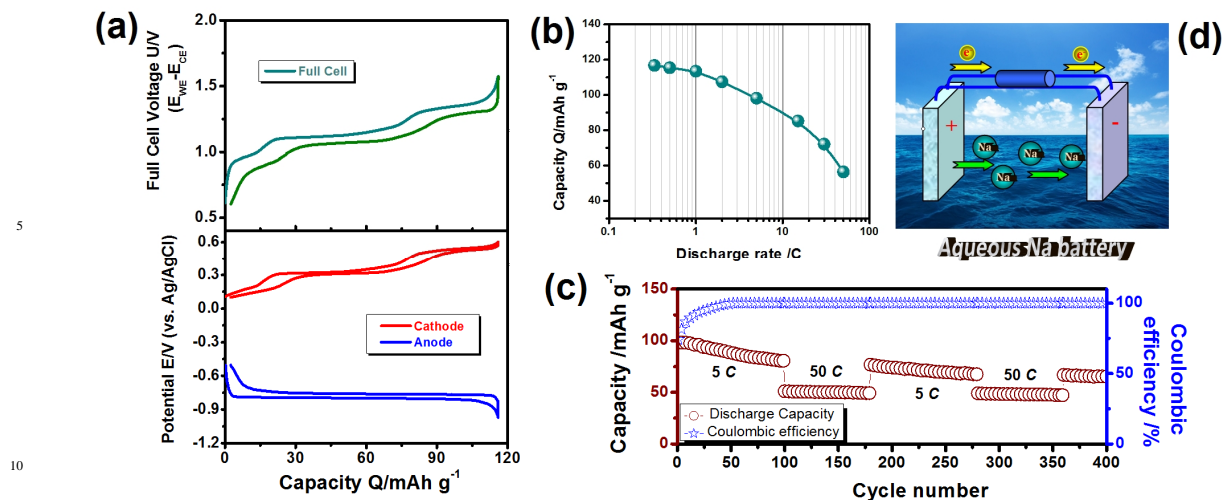
Figure 8 (a) Charge/discharge curves of the full cell, the $Na_{0.44}MnO_2$ cathode and the wafer-like $NaTi_2(PO_4)_3$ anode at the 1 *C* rate. The rate capability (b) and long-term cycling property (c) of the aqueous rechargeable cell under different current densities. (d) Schematic image of the electrochemical process in aqueous rechargeable sodium battery is also shown.

Furthermore, an aqueous rechargeable sodium battery is assembled using $Na_{0.44}MnO_2$ as cathode, wafer-like $NaTi_2(PO_4)_3$ as anode and 1M Na_2SO_4 as electrolyte (Figure 8d). A reference Ag/AgCl electrode is employed to monitor the potential change for individual electrode during charge/discharge process. Figure 8(a) displays the charge/discharge curves of the cathode, anode and the full cell at the 1 *C* rate. The flat potential plateaus of $NaTi_2(PO_4)_3$ anode are associated with the redox reaction of Ti^{3+}/Ti^{4+} as discussed above. The three separate plateaus of the $Na_{0.44}MnO_2$ cathode are attributed to the phase transitions upon sodium de/intercalation process, which accords well with the results of previous reports[38]. The full cell delivers the capacity of 113.5 mAh g^{-1} with respect to anode active materials. As current density increases, the capacities decrease correspondingly. The rate capability of the full cell under different current densities is summarized in Figure 8(b). Even at the current density as high as 30 *C*, the retained capacity remains more than 64% of that for discharging at the 1 *C* rate, demonstrating its ultrafast charge/discharge capability. Our result is comparable to previous report[7] when the current density is lower than 10 *C*. However it is slightly inferior to that as the current density is even higher, which maybe associated with the insufficient optimization of the design for the full cell. Thus great efforts are still needed for further improvement. Figure 8(c) shows the long term cycling performance of the full cell. After 400 cycles at alternate 50 and 5 *C* rates, the cell still retains about 67% of the capacity of initial cycle. The change of coulombic efficiency for the full cell during cycles is similar to that of the wafer-like $NaTi_2(PO_4)_3$ electrode. After increases in the initial cycles, the coulombic efficiency of the full cell finally stabilizes at nearly 100% during cycles. Based on above results, it demonstrates that wafer-like $NaTi_2(PO_4)_3$/C composite is a good anode candidate for constructing high performance aqueous rechargeable sodium batteries.

4 Conclusions

In summary, a wafer-like porous architecture decorated by hierarchical carbon has been designed and fabricated to develop high-performance electrode materials. The crystals are coated by a nanoscale carbon layer and wrapped by a microscale carbon network, which constructs the high conductive and high porous wafer-like structure for fast electron/ion transport. As a case study, the wafer-like $NaTi_2(PO_4)_3$/C composite is prepared by a self-assemble synthesis. Both CV and galvanostatic charge/discharge results demonstrate its improved sodium intercalation capability and superior high rate capability. Moreover, a full aqueous rechargeable sodium battery is fabricated using wafer-like $NaTi_2(PO_4)_3$ as anode and $Na_{0.44}MnO_2$ as cathode. The cell delivers outstanding high rate capacity and ultralong-life cycling performance, which retains 67% of the capacity after 400 cycles at alternate 50 and 5 *C* rates. Even at 30 *C*, it still delivers 64% of the capacity. The superior high rate capability is attributed to the synergistic effects of bicontinuous electron pathways, large electrode/electrolyte interfaces and robust structure stability for the wafer-like structure. Therefore, the present hierarchical carbon decorated wafer-like structure is a promising alternative to construct high performance electrode for ARSB.

Acknowledgements

Notes and references

[a]Key Laboratory for Photonic and Electronic Bandgap Materials, Ministry of Education; College of Chemistry and Chemical Engineering, Harbin Normal University, Harbin, 150025, Heilongjiang, China; E-Mail: chaodenghsd@sina.com

b Key Laboratory of Superlight Material and Surface Technology, Ministry of Education, College of Material Science and Chemical Engineering, Harbin Engineering University, Harbin 150001, Heilongjiang, China; E-Mail: senzhang@hrbeu.edu.cn

1   J. M. Tarascon, M. Armand, *Nature*, 2001, **4**, 359.

2   P. Barpanda, M. Ati, B. C. Melot, G. Rousse, J. N. Chotard, M. L. Doublet, M. T. Sougrati, S. A. Corr. J. C. Jumas, J. M. Tarascon, *Nat. Mater.*, 2011, **10**, 772.

15 3   M. S. Whittingham, *Chem. Rev.*, 2004, **104**, 4271.

4   S. Zhang, C. Deng, H. Gao, F. L. Meng, M. Zhang, *Electrochim. Acta*, 2013, **107**, 406.

5   W. Li, J. R. Dahn, D. S. Wainwright, *Science*, 1994, **264**, 1115.

6   H. Kim, J. Hong, K. Y. Park, H. Kim, S. W. Kim, K. Kang, *Chem. Rev.*, 2014, **114**, 11788.

7   Z. Li, D. Young, K. Xiang, W. C. Carter, Y. M. Chiang, *Adv. Energy Mater.*, 2013, **3**, 290.

8   F. Sauvage, L. Laffont, J. M. Tarascon, E. Baudrin, *Inorg. Chem.*, 2007, **46**, 3289.

25 9   C. Deng, S. Zhang, Y. X. Wu, *Nanoscale*, 2015, **7**, 487.

10   X. Y. Wu, M. Y. Sun, Y. F. Shen, J. F. Qiang, Y. L. Cao, X. P. Ai, H. X. Yang, *ChemSusChem*, 2014, **7**, 407.

11   Z. Hou, X. Li, J. Liang, Y. Zhu, Y. Qian, *J. Mater. Chem. A*, 2015, **3**, 1400.

30 12   M. Pasta, C. D. Wessells, N. Liu, J. Nelson, M. T. Mcdowell, R. A. Huggins, M. F. Toney, Y. Cui, *Nat. Commun.*, 2014, **5**, 3007.

13   C. Deng, S. Zhang, Z. Dong, Y. Shang, *Nano Energy*, 2014, **4**, 49.

14   Q. T. Qu, L. L. Liu, Y. P. Wu, R. Holze, *Electrochim. Acta*, 2013, **96**, 8.

35 15   S. I. Park, I. Gocheva, S. Okada, J. I. Yamaki, *J. Electrochem. Soc.*, 2011, **158**, A1067.

16   G. Pang, C. Z. Yuan, P. Nie, B. Ding, J. J. Zhu, X. G. Zhang, *Nanoscale*, 2014, **6**, 6328.

17   W. Wu, A. Mohamed, J. F. Whitacre, *J. Electrochem. Soc.*, 2013, **40** **160**, A497.

18   X. N. Li, X. B. Zhu, J. W. Liang, Z. G. Hou, Y. Wang, N. Lin, Y. C. Zhu, Y. T. Qian, *J. Electrochem. Soc.*, 2014, **161**, A1181.

19   W. Wu, J. Y. Yan, A. Wise, A. Rutt, J. F. Whitacre, *J. Electrochem. Soc.*, 2014, **161**, A561.

45 20   S. Xin, Y. G. Guo, L. J. Wan, *Acc. Chem. Res.*, 2012, **45**, 1759.

21   L. Tan, S. Zhang, C. Deng, *J. Power Sources*, 2015, **275**, 6-13.

22   C. Deng, S. Zhang, L. Ma, Y. H. Sun, S. Y. Yang, B. L. Fu, F. L. Liu, Q. Wu, *J. Alloys Compd.*, 2011, **509**, 1322.

23   Y. Xia, Z. Xiao, X. Dou, H. Huang, X. H. Lu, R. J. Yan, Y. P. Gan, 50 W. J. Zhu, J. P. Tu, W. K. Zhang, X. Y. Tao, *ACS Nano*, 2013, **7,** 7083.

24   C. Deng, S. Zhang, H. Gao, M. Zhang, F. L. Meng, *J. Electroanal. Chem.*, 2014, **719**, 150.

25   D. Han, S. Lim, Y. Kim, S. Kang, Y. Lee, Y. Kang, *Chem. Mater.*, 55 2014, **26**, 3644.

26   X. N. Lu, Y. Shang, S. Zhang, C. Deng, *Electrochim. Acta*, 2015, **155**, 148.

27   S. Zhang, C. Deng, F. L. Liu, Q. Wu, M. Zhang, F. L. Meng, H. Gao, *J. Electroanal. Chem.*, 2013, **689**, 88.

60 28   Y. M. Sun, X. L. Hu, F. F. Xia, Y. H. Huang, *Adv. Funct. Mater.*, 2013, **23**, 2436.

29   S. Zhang, C. Deng, Y. Meng, *J. Mater. Chem. A*, 2014, **2**, 20538.

30   Y. Meng, S. Zhang, C. Deng, *J. Mater. Chem. A*, 2015, **3**, 4484.

31   S. Kim, H. Jeong, J. Kwon, I. Ock, W. Suh, G. Stucky, J. Kang, 65 *Energy Environ. Sci.*, 2015, **8**, 188.

32   C. Zhang, Z. Chen, Z. Guo, X. Lou, *Energy Environ. Sci.*, 2016, **6**, 974.

33   Y. Z. Luo, X. Xu, Y. X. Zhang, Y. Q. Pi, Y. L. Zhao, X. C. Tian, Q. Y. An, Q. L. Wei, L. Q. Mai, *Adv. Energy Mater.*, 2014, **4**, 70 1400107.

34   Q. Y. Wang, B. D. Zhao, S. Zhang, X. H. Gao, C. Deng, *J. Mater. Chem. A*, 2015, **3**, 7732.

35   W. T. Gu, A. Magasinski, B. Zdyrko, G. Yushin, *Adv. Energy Mater.*, 2015, **5**, 1401148.

75 36   A. Ferrari, J. Robertson, *Phys. Rev. B: Condens. Matter Mater. Phys.*, 2000, **61**, 14095.

37   A. Bard, L. R. Faulkner, *Electrochemical Methods*, Wiley press, New York, 2nd edn, 2001.

38   D. J. Kim, R. Ponraj, A. G. Kannan, H. W. Lee, R. Fathi, R. Ruffo, 80 C. M. Mari, D. K. Kim, *J. Power Sources*, 2013, **244**, 758.